Unveiling transport properties of Co2MnSi Heusler epitaxial thin films with ultra-low magnetic damping

C. de Melo, C. Guillemard, A.M. Friedel, V. Palin, J.-C. Rojas-Sánchez, S. Petit-Watelot, Stéphane Andrieu

Unveiling transport properties of Co_2MnSi Heusler epitaxial thin films with ultra-low magnetic damping

C. de Melo [a,b], C. Guillemard [a,c,1], A. M. Friedel [a,d], V. Palin [a,c], J. C. Rojas-Sánchez [a], S. Petit-Watelot [a] and S. Andrieu [a]

[a] Institut Jean Lamour, UMR CNRS 7198, Université de Lorraine, 54000 Nancy, France

[b] Chair in Photonics, LMOPS EA 4423 Laboratory, CentraleSupélec, Université de Lorraine, 57070 Metz, France

[c] Synchrotron SOLEIL-CNRS, L'Orme des Merisiers, 91192 Gif-sur-Yvette, France

[d] Fachbereich Physik and Landesforschungszentrum OPTIMAS, Technische Universität Kaiserslautern, 67663 Kaiserslautern, Germany

ABSTRACT

The family of Co-based Heusler compounds contains promising candidates for spintronic applications regarding their predicted Half-Metal-Magnetic nature, ultra-low magnetic damping coefficients, high curie temperatures and tunable electronic properties. Here we focused on the transport properties of Co_2MnSi thin films with thickness in the range of 4-44 nm exhibiting magnetic damping in the 10^{-4} range. The goals of this study are to examine the impact of the peculiar electronic band structure on the transport properties, to identify the temperature-dependent scattering process, and to extract robust conduction parameters to exploit this material in magnetoelectric devices. In order to undoubtedly correlate all results, the full study has been performed on the same series of samples. Scanning transmission electron microscopy experiments were performed to check the chemically-ordered $L2_1$ phase in our films, and also allowed us to identify misfit dislocations generated at the interface with the substrate. The variation of the resistivity with film thickness was measured at different temperatures. The results are examined under the Fuchs and Sondheimer model which allowed us to extract the electron mean free path in Co_2MnSi in the temperature range 5 – 300 K. Values for the residual resistivity, Debye temperature, and distance between the Fermi energy and the conduction band for minority spins were obtained from the fit of the resistivity versus temperatures curves. A negative AMR ratio was measured for all the samples which confirmed the Half-metallic nature of the Co_2MnSi films. The determination of the ordinary Hall coefficient alloys allowed us to extract the carrier concentration and carrier mobility and their dependency on the temperature. Finally, scaling of the anomalous Hall coefficient with the longitudinal resistivity was performed indicating that skew scattering is the dominant temperature-dependent scattering mechanism in our films.

---

[1] ALBA Synchrotron Light Source, Barcelona 08290, Spain.

Corresponding authors : claudia.de-melo@univ-lorraine.fr

stephane.andrieu@univ-lorraine.fr

Keywords: Heusler alloys, Co_2MnSi, electrical resistivity, anisotropic magnetoresistance, Hall effect, magnetic damping.

1. INTRODUCTION

X_2YZ Heusler intermetallic compounds, where X and Y are transition or rare-earth metals while Z is a main-group element (s or p-block in the periodic table), have attracted a lot of attention since their discovery by F. Heusler in 1903 [1]. The broad family of Heusler compounds find applications in a variety of fields like spintronic, magneto-optics, thermoelectricity, magnonics, superconductivity, among others [2–4]. Even today, these materials constitute an active field of research with the emergence of new functionalities and prospective applications, for example, the discovery of the Half-Heusler topological insulators [5,6] or the recent observation of single pulse all-optical switching in the Mn_2Ru_xGa Heusler compound [7].

An interesting class of Heusler compounds are the half metal ferromagnets (HMF), that were discovered by Groot *et al.* in 1983 [8]. In these materials, the majority spin band has a typical metallic behavior while the minority spin band possesses an insulating or semiconducting character due to the existence of a bandgap around the Fermi energy. Therefore, HMF are 100% spin polarized at the Fermi energy with the potential to generate fully spin-polarized currents, which is highly desirable to improve the efficiency and functionalities of magnetoresistive devices [9]. Furthermore, due to the lack of minority spin density of states at the Fermi energy, ultra-low magnetic damping coefficients have been predicted ($\sim 10^{-4} - 10^{-5}$) for these materials [10,11], which are highly sought for magnonic applications, spin-transfer-torque and spin-orbit-torque-based devices [12,13].

Co-based Heusler compounds are a very promising class of HMF since together with the half-metallicity and low magnetic damping coefficients [14–17] they possess high Curie temperatures well above room temperature, tunable band structure [14] and lattice constants close to some commercial semiconductors like GaAs and Si, which favor their possible integration in semiconductors industry [18]. Among the 3d-transition-elements-based Heusler compounds, Co_2MnSi is a promising candidate for spintronic applications due to its large bandgap for minority spins (0.5 to 0.8 eV) [14]. The existence of a minority spin gap and 100% spin polarization has been demonstrated for this compound by spin-resolved photoemission spectroscopy [19,20]. Furthermore, we measured ultra-low magnetic damping coefficients with a record value equal to $4.6 * 10^{-4}$ at 300 K, which is the lowest value reported so far for a conductive material [14]. Tunnel magnetoresistance (TMR) ratios as high as 1995 % and 354 % have been reported for epitaxial Co_2MnSi/MgO/Co_2MnSi magnetic tunnel junctions at low and room temperature, respectively [21]. Large magnetoresistance ratios over 30% at room temperature and over 60 % at low temperatures have also been reported for current perpendicular-to-plane giant magnetoresistance (CPP-GMR) devices with Co_2MnSi as ferromagnetic electrode [22]. However, the electronic properties and the half-metallicity seem to be very sensitive to the structure and composition of the films [23], which can negatively impact the physical properties and the performance of these films when implemented in CPP – GMR or TMR magnetoresistive devices.

In this work, we report on the transport properties of Co_2MnSi epitaxial thin films deposited on MgO substrates by molecular beam epitaxy, which allows a precise control of films' stoichiometry [23]. This allows us to get systematically magnetic damping in the 10^{-4} – 10^{-3} range for this compound, at least for film thicknesses above 5 nm. The crystalline quality of the

films was monitored by electron diffraction, X-ray diffraction and transmission electron microscopy. Particular attention was paid to the possible presence of dislocations due to the mismatch between the film and the substrate since such defects may play a role in transport properties. The electronic transport properties in these films were then explored by performing resistivity measurements on a series of films with thickness varying in the range 4 – 44 nm. The resistivity versus thickness measurements were examined using the Fuchs-Sondheimer analysis in order to extract important parameters like the electron mean free path. The resistivity dependence with temperature in the 5 – 300 K range was also analyzed and compared to models taking into account the spin gap in this compound. Magneto-transport measurements were also systematically performed on the sample series. Negative Anisotropic Magneto-Resistance (AMR) values were obtained and explained as a consequence of the half-metallic nature of the films. Hall measurements were done to determine the carrier mobility and carrier concentration and to study their dependency on temperature and film thickness. The temperature dependence of the Anomalous Hall Effect (AHE) was analyzed to go deeper in understanding the scattering process in these films.

2. STRUCTURAL AND MAGNETIC PROPERTIES OF THE FILMS

The Co_2MnSi (CMS) films were deposited on MgO (001) substrates by molecular beam epitaxy. The 3 elements were co-evaporated and each atomic flux was controlled with a ± 1 % accuracy (see [23] for more details). The Co_2MnSi layers grow on (001) MgO substrates with (001) [110] Co_2MnSi || (001) [100] MgO epitaxial relationship (Fig. 1). The thickness of the films was tuned in the range 4 - 44 nm and the films were protected from oxidation by a 2 nm Au-capping layer. X-ray diffractograms of the samples are presented in Fig. 1a, showing the Co_2MnSi (002) and (004) peaks and the (111) crystallographic planes of the Au-capping layer.

To extract the in-plane lattice parameter of Co_2MnSi, (422) crystallographic planes were measured in a non-symmetrical configuration (see supplementary information Figure S1). The in-plane and out-of-plane lattice parameters were thus extracted from (004) and (422) peaks and a similar lattice parameter was measured for all the thickness series except for the 4 nm sample for which a small deviation is noticeable (Fig. 1b).

Since X-ray diffraction at a fixed wavelength is not sufficient to unambiguously determine the chemical ordering [23], Scanning Transmission Electron Microscopy experiments were performed using the High-Angle Annular Dark-Field technique (STEM- HAADF) along the [110] zone axis. A special pattern is thus expected for the $L2_1$ structure [23] along this zone axis which is actually observed in the whole thickness of the films as shown in Fig. 1c. This technique was also exploited to look at possible structural defects like misfit dislocations expected in this kind of hetero-epitaxial Co_2MnSi on MgO system presenting a -4.9 % lattice misfit. According to heteroepitaxial theory [24,25], the distance between interfacial dislocations is given by the relationship $a_{\mathrm{MgO}}(100) * m \approx d_{\mathrm{CMS}}(110) * (m+1)$, where m is an integer, $d_{\mathrm{CMS}}(110)$ is the interplanar distance of the (110) crystallographic planes of Co_2MnSi. This gives $m \approx 19$, meaning that the distance between misfit dislocations should be observed around this value. In order to evidence the dislocations, a Fast Fourier transform (FFT) of the TEM image was performed at the interface between Co_2MnSi and MgO (violet frame in Fig. 1c). The (220) and $(\bar{2}\bar{2}0)$ Co_2MnSi diffraction spots were thus selected (Fig. 1d) and inverse-FFT of the masked planes was performed, obtaining the image in Fig. 1e. The misfit dislocations marked by dotted circles in Fig. 1e are clearly visible. These dislocations were observed along the Co_2MnSi/MgO interface, with a similar distribution for all Co_2MnSi thickness series. From the analysis of several interface images, the distance between dislocations was observed to vary from

$m = 17$ to 21, in good agreement with misfit dislocation theory. The presence of this dislocations network at the interface explains why the lattice spacing slightly deviates from the bulk value for low thicknesses as shown in Fig. 1b. Such structural defects have to be considered when interpreting conduction properties as presented in the following.

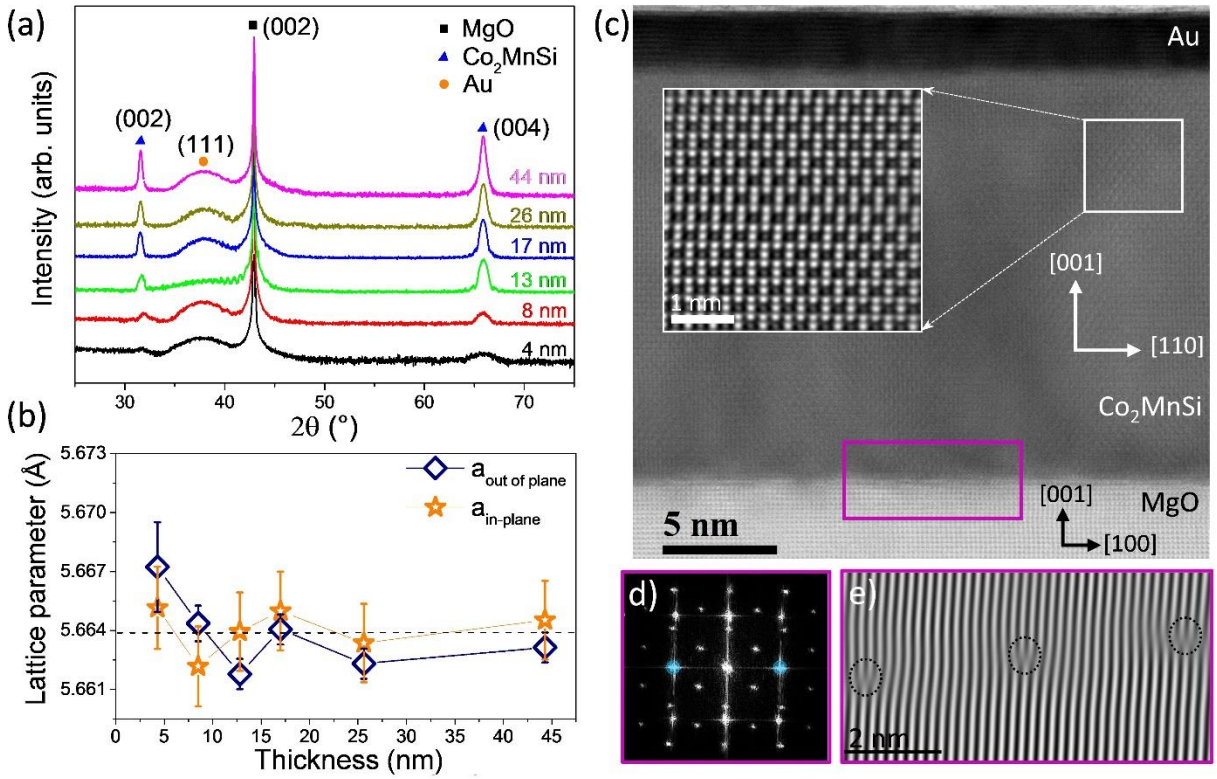

Fig. 1. Structural characterization of the Co_2MnSi films. (a) X-ray diffraction patterns of the Co_2MnSi thickness series in the Bragg-Brentano configuration. (b) Lattice parameter of the Co_2MnSi thickness series: in-plane (orange stars) and out-of-plane (blue diamonds), obtained from (004) and (422) reflections, respectively. (c) STEM micrograph of the 17 nm Co_2MnSi film along the $[1\bar{1}0]$ zone axis. A filtered STEM-HAADF micrograph performed in the region enclosed by a white frame is shown as inset. (d) Fast Fourier transform (FFT) image performed at the interface between CMS and MgO (violet frame in c). (e) Inverse-FFT image of the masked planes (cyan circles) in the FFT pattern shown in (d). The dislocations at the interface are highlighted by dotted circles.

The magnetic damping and effective magnetization of the Co_2MnSi films were extracted from ferromagnetic resonance (FMR) measurements. This is a powerful technique for verifying the quality of the films and for ruling out the existence of multiple phases and/or stoichiometry issues [23]. Ferromagnetic resonance (FMR) measurements were performed in a Physical Properties Measurement System (PPMS) equipped with a PhaseFMR-40 system. The measurements were performed at 300 K with the magnetic field applied perpendicular to the film plane to avoid two-magnon scattering contributions. The microwave frequency was kept fixed and the magnetic field was swept, starting from the highest field to guarantee the saturation of the films' magnetization. Multiple measurements were performed at different frequencies ranging from 10 to 40 GHz (see supplementary information Figure S2). The effective magnetization and the effective magnetic moment per formula units (f.u.) were extracted from the fit of the microwave frequency vs. resonance field, and the Gilbert damping (α) and inhomogeneous linewidth (ΔH_0) from the fit of resonance linewidth (ΔH) vs. microwave frequency. The inhomogeneous linewidth Δf_0 can be obtained from ΔH_0 by the Larmor equation: $f = \frac{\gamma}{2\pi}\mu_0 H$, where $\gamma/2\pi$ is the gyromagnetic ratio. The obtained values are reported in Table I. As can be seen, the effective magnetization of the films increases with increasing film thickness, reaching the highest value of 1.33 T for the 44 nm film. In general, the effective magnetization of the films fits well to the theoretical expected value for Co_2MnSi of 5 μ_B/f. u. (1.28 T) except for the thinnest films where slightly smaller values were obtained. The evolution of the effective magnetization is discussed in supplementary information section 2.

Most of the samples showed ultra-low magnetic damping coefficients in the $10^{-3} - 10^{-4}$ range (see Table I). It is worth to mention that the damping coefficients reported here are the raw effective values containing the intrinsic and extrinsic contributions (see details in the

supplementary information section 2). There exist some approaches to separate the different damping contributions and to extract the intrinsic damping coefficient [26,27]. However, we prefer to report here the global values, which represent upper limits, but most realistic ones for comparisons. The magnetic damping of the Co_2MnSi thickness series increases with the increase of film thickness from 8 to 44 nm (Table I). We believe that this is due to the extrinsic damping contributions, that originates from Eddy currents induced in the sample (α_{eddy}) and Eddy currents induced in the waveguide, known as radiative damping (α_{rad}), since both contributions increase with increasing film thickness ($\alpha_{eddy} \sim t^2/\rho(t)$, and $\alpha_{rad} \sim t$ [28]). This hypothesis is supported by the increase of FMR lineshape asymmetry that was observed with the increase of film thickness which is a signature of the presence of Eddy currents in the samples [29] (see supplementary information Figure S2). It is worth to mention that the damping coefficients reported here are slightly higher than the values reported in our previous work for the sample of the same thickness [14]. However, the measurements reported here were performed in a different experimental setup with a waveguide of larger dimensions implying a higher sensitivity to inhomogeneities, that can also contribute to an increase of the intrinsic damping since this technique is very sensitive to even small deviations from the 2:1:1 stoichiometry [23]. The fact that the extrinsic contributions depend on the waveguide geometry may also affect the measured damping coefficients. The inhomogeneous linewidth (FWHM) of the films, Δf_0, increases with the decrease of film thickness (Table I). This parameter is related with inhomogeneities of the magnetic phase and with the existence of local defects in the films. Therefore, the misfit dislocations observed in the STEM micrograph (Fig. 1e) are a source of inhomogeneous linewidth. Since these defects were only observed at the Co_2MnSi/MgO interface and not in the bulk of the Co_2MnSi layer, their impact should become more relevant with the decrease of film

thickness due to the increase of the relative amount of defects, and this is what we observe from FMR measurements. Finally, the Landé factor (g) was obtained from the linear fit of the microwave frequency vs. resonance field mentioned above, through the relation: $g = h\,\gamma/2\pi\,\mu_B$, where h is the Plank constant, $\gamma/2\pi$ is the gyromagnetic ratio, and μ_B is the Bohr magneton. The g values were practically constants through all the thickness series and they are close to the free electron value ($g = 2.0023$) as expected for 3d compounds (Table I).

Table I. Effective magnetization (relative error of ~1%), magnetic damping (α), inhomogeneous linewidth in field ($\mu_0\Delta H_0$) and frequency (Δf_0) and Landé g-factor, extracted from FMR measurements performed on the Co_2MnSi thickness series.

Co_2MnSi thickness (nm)	$\mu_0 M_{eff}$ (T) / (μ_B/f. u.)	α (10^{-4})	$\mu_0\Delta H_0$ (mT)	Δf_0 (MHz)	g
4	1.15 / 4.51	20.9 ± 0.6	3.12 ± 0.11	88 ± 3	2.01 ± 0.01
8	1.19 / 4.64	7.8 ± 0.3	1.73 ± 0.07	49 ± 2	2.03 ± 0.02
13	1.26 / 4.92	8.9 ± 0.1	0.88 ± 0.03	24.9 ± 0.7	2.02 ± 0.01
21	1.22 / 4.77	9.3 ± 0.2	0.46 ± 0.05	13.1 ± 1.4	2.02 ± 0.01
44	1.33 / 5.20	15.6 ± 0.4	0.43 ± 0.07	12.2 ± 1.9	2.03 ± 0.01

3. TRANSPORT PROPERTIES

For the transport measurements the films were patterned into Hall bars of lateral dimension 4 µm×32 µm, along the CMS - [110] direction by standard UV-photolithography and subsequent ion beam etching. Ti (10 nm) /Au (150 nm) contact pads were deposited by electron beam evaporation. Transport measurements were performed using the standard 4-points probe technique in a Quantum Design Physical Property Measurement System (PPMS). As indicated in Fig. 2a, the current (i) was injected along the [110]-CMS direction between contacts pad A-B and the voltage drop was measured between contacts pad C-D for longitudinal resistivity (ρ_{xx}) or D-E for Hall voltage measurements (ρ_{xy}). Anisotropy Magneto Resistance (AMR)

measurements were performed by applying an in-plane magnetic field between $\pm$ 100 mT, which is enough to saturate the magnetization of the Co_2MnSi films in-plane (see supplementary information Figure S4a). The AMR ratio was calculated from the difference in the film resistivity in the parallel ($H \parallel i$) and perpendicular ($H \perp i$) configurations by rotating the magnetic field by 90° in-plane. Hall measurements were performed by sweeping the magnetic field applied perpendicular to the film plane, from -6 T to 6 T, to extract the ordinary and anomalous Hall coefficients.

3.1. Electrical Resistivity

Due to the Au-capping layer, the measured resistance is the equivalent resistance of the bi-layer system composed by Au and Co_2MnSi. Considering the bi-layer system as two parallel conductors the equivalent sheet resistance (R_{sheet}) can be expressed as the individual sheet resistance in each CMS (R_{CMS}) and Au (R_{Au}) layer:

$$1/R_{sheet} = 1/R_{CMS} + 1/R_{Au}, \quad \text{with} \quad R_{CMS} = \rho_{CMS}/t \qquad (1)$$

where ρ_{CMS} and t are the resistivity and thickness of the CMS films. In the following, the resistivity measurements are analyzed into two ways. First, *the R_{sheet} variation with the film thickness at a fixed temperature* was studied through conduction models that take into account scattering in the film and at the interface / surface. Second, we analyzed *the R_{sheet} variation with temperature for a fixed thickness*, by considering the different resistivity contributions coming from intrinsic resistivity (defects), magnonic and phononic processes.

The R_{sheet} (and $1/R_{sheet}$ in inset) is plotted as a function of film thickness in Fig. 2c for two fixed temperatures, 300 K and 5 K. The increase of resistance at low thicknesses is due to the scattering of conduction electrons at the film surface and interface, which is enhanced when the

film thickness becomes smaller than the mean free path of electrons in the material. The bulk resistivity (ρ_B) and the electron mean free path (λ) were thus extracted by fitting the sheet resistance vs. thickness (t). According to the Fuchs and Sondheimer model [30], the Co_2MnSi resistivity dependence with thickness can be expressed as :

$$R_{CMS} = \frac{\rho_B}{t}\left[1 + \frac{3}{4}\left(q - \frac{q^3}{12}\right) * I(q) - \frac{3}{8\,q}(1 - e^{-q}) - \left(\frac{5}{8} + \frac{q}{16} - \frac{q^2}{16}\right) e^{-q}\right]^{-1} \qquad (2)$$

where $q = t/\lambda$ and $I(q)$ is the exponential integral $\left(I(q) = \int_q^\infty \frac{e^{-x}}{x} dx\right)$. We thus proceeded in a fitting of R_{sheet} using eq. (1) and eq. (2), by varying 3 parameters, i.e. ρ_B, λ and R_{Au}. The fitting curves are in very good agreement with experimental data, as shown in Fig. 2c. The extracted parameters are listed in Table II. It should be noted that the extracted ρ_B values are in good agreement with the residual resistivity reported for epitaxial Co_2MnSi thin films [31,32]. Our analysis allows us to go further by determining the electron mean free path in Co_2MnSi in the temperature range 5 – 300 K.

Eq. (2) can be modified to account for partial elastic scattering at the film surface/interface [30]. Fitting of the experimental data including a factor p, that represents the fraction of specular surface collisions, results in an increase of the electron mean free path when increasing p. Since the estimation of this parameter is not straightforward, we only consider the simple case of purely inelastic scattering ($p = 0$), which means that the values of λ obtained here represent a lower limit for the electron mean free path in Co_2MnSi.

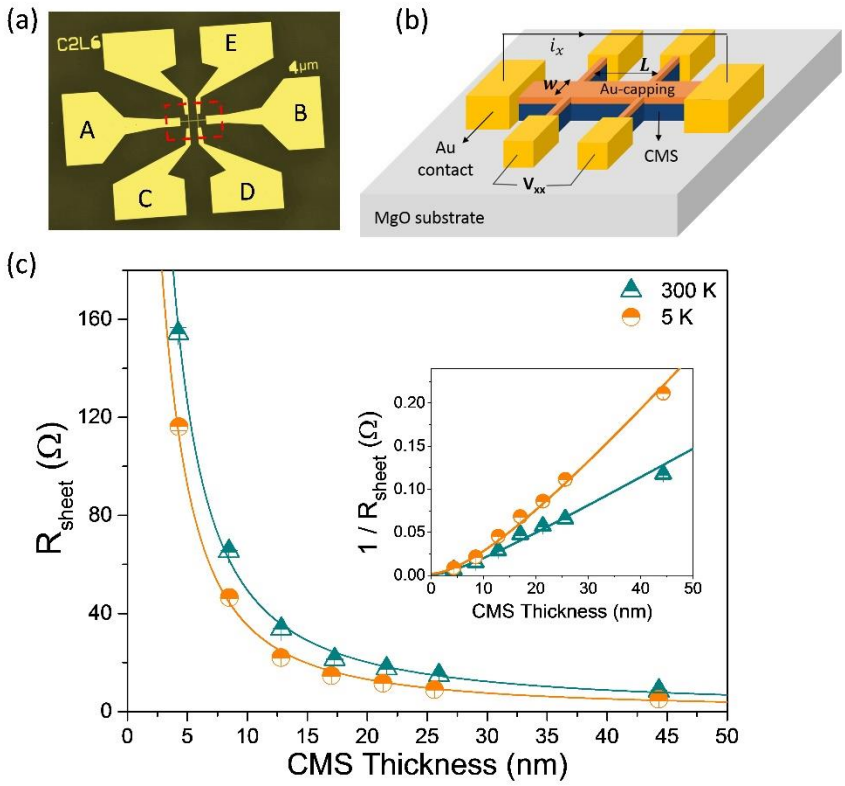

Fig. 2. Patterning and electrical characterization of the films. (a) Top-view optical image of the sample: Hall bar geometry used for transport measurements. (b) Schematic of the device and contact geometry. (c) Equivalent sheet resistance of the samples (CMS + Au) versus CMS thickness at 300 K (triangles) and 5 K (circles). Solid lines correspond to the fitting with the Fuchs and Sondheimer model (eq. 1, 2). Inverse of the equivalent sheet resistance is shown in the inset.

Table II. Bulk resistivity, ρ_B (error ~ 8 %), electron mean free path, $\boldsymbol{\lambda}$ (error ~ 15 %), Au sheet resistance, R_{Au} (error ~ 17 %), for Co_2MnSi at different temperatures from 5 to 300 K.

Temperature (K)	$\boldsymbol{\rho_B}$ **(μΩ cm)**	$\boldsymbol{\lambda}$ **(nm)**	$\boldsymbol{R_{Au}}$ **(Ω)**
5	14.8	36	489
50	15.6	32	510
100	18.1	26	650
150	25.3	21	936
250	22.0	20	900
300	31.5	14	1116

We now focus our analysis on the temperature effect for a given thickness. The electrical resistivity of a ferromagnetic metal can be separated in three main contributions: the residual resistivity (ρ_r) independent of temperature, coming from the scattering of electrons with the impurities and imperfections of the crystal lattice, the phononic contribution (ρ_{ph}) arising from the scattering of electrons with the lattice vibrations, and the magnonic contribution due to scattering of electrons with the magnetic spin system (ρ_m). In general, the magnonic contribution has a quadratic dependency with temperature. However, the electron-magnon scattering is expected to decrease exponentially with temperature in HMF due to the suppression of spin-flip as a result of the existence of a gap in one of the spin bands. As a consequence, the following expression is typically employed to account for the magnonic contribution in HMF [33,34]:

$$\rho_m = A * T^2 e^{-\Delta/k*T} \quad (3)$$

where A is a constant that represents the strength of electron-magnon scattering, T the temperature, k the Boltzmann constant, and Δ the separation between the Fermi energy and the first available states at the minority spin band. The phononic contribution can be described by the Bloch-Grüneisen ($n = 5$) or Bloch-Wilson ($n = 3$) formula, as follows:

$$\rho_{Ph}(T) = \mathrm{B} * \left(\frac{T}{\Theta_D}\right)^n \int_0^{\Theta_D/T} \frac{x^n}{(e^x-1)*(1-e^{-x})} dx \quad (4)$$

where B is a constant, Θ_D the Debye temperature, and n indicates the electron-phonon scattering mechanism contributing to the resistivity of the films: n=5 for intraband $s-s$ scattering and n=3 for interband $s-d$ scattering [35]. Therefore, the final expression for the resistivity of the films is:

$$\rho_{CMS} = \rho_r + \rho_m(T) + \rho_{ph}(T,n) = \rho_r + A * T^2 e^{-\Delta/kT} + \mathrm{B} * \left(\frac{T}{\Theta_D}\right)^n \int_0^{\Theta_D/T} \frac{x^n}{(e^x-1)*(1-e^{-x})} dx \quad (5)$$

We can now analyze our experimental results by considering these different mechanisms. To get experimental ρ_{CMS} we subtracted the Au contribution obtained from the fit with eq. (1). Then we

proceed to fit the ρ_{CMS} by varying 6 parameters, i.e. ρ_r, A, Δ, B, Θ_D, and n was allowed to take the values 3 or 5. Fig. 3a shows the Co_2MnSi resistivity, ρ_{CMS}, as a function of the temperature from 5 to 300 K, the dotted lines being the fit to eq. (5). The ρ_r, Θ_D and Δ extracted values are reported in Table III for the entire thickness series.

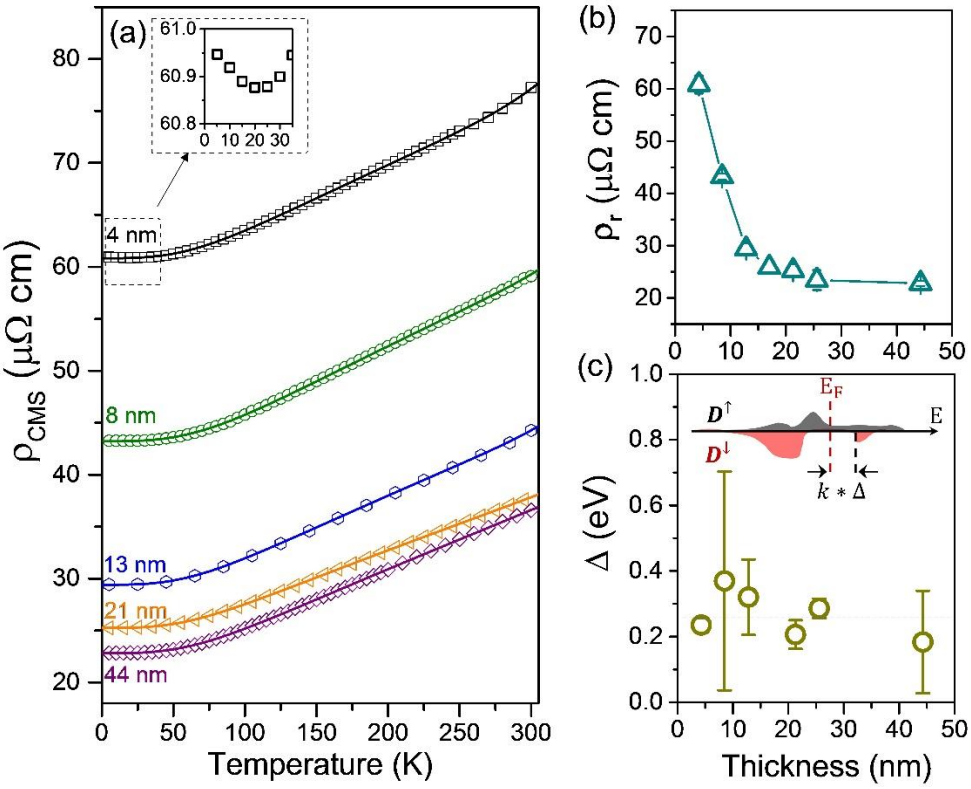

Fig. 3. Evolution of CMS resistivity with temperature. (a) Resistivity versus temperature for the Co_2MnSi thickness series. Solid lines are the fits to experimental data with eq. (5). In the inset, a zoom of the ρ_{CMS}(T) curve in the low-temperature range for the 4 nm Co_2MnSi film is shown. (b) Co_2MnSi residual resistivity versus thickness. (c) Distance between the Fermi energy and the bottom of the minority spin conduction band, Δ, obtained from the fit of ρ_{CMS} vs. T with eq. (5) for the entire thickness series. A schematic of the DOS for both spins is shown as an inset.

Table III. Residual resistivity ρ_r, energy Δ of the minority spin conduction band relative to the Fermi energy, and Debye temperature Θ_D extracted from the fits shown in Fig. 3a using eq. (5) for n=3.

Co_2MnSi thickness (nm)	ρ_r (μΩ*cm)	Δ (eV)	Θ_D (K)
4	60.8 ± 0.1	0.23 ± 0.02	477 ± 3
8	43.2 ± 0.2	0.36 ± 0.30	493 ± 8
13	29.4 ± 0.2	0.32 ± 0.10	477 ± 6
21	25.3 ± 0.1	0.21 ± 0.04	457 ± 1
26	23.4 ± 0.1	0.29 ± 0.03	483 ± 2
44	22.8 ± 0.1	0.18 ± 0.15	485 ± 2

This analysis considering eq. (5) leads to several conclusions:

(i) The fits of Co_2MnSi resistivity vs. temperature without taking into account the magnonic contribution already reproduce the experimental data fairly well, which means that the principal contribution to the resistivity of the films is coming from electron-phonon scattering, at least in the range of temperature studied here.

(ii) A superior fit was obtained with $n = 3$ for all the samples indicating that $s - d$ scattering is the predominant contribution to the films' resistivity.

(iii) In this analysis, the thickness dependence is included in the residual resistivity ρ_r. It is thus not surprising to observe similar $\rho_r(t)$ and $R_{sheet}(t)$ curves (respectively in Fig. 3b and Fig. 2c). Nevertheless, this term is certainly also affected by the dislocations network observed in the STEM micrographs (Fig. 1e) for the entire thickness series. Since these defects were only observed at the Co_2MnSi and MgO interface and not in the bulk of the Co_2MnSi layer, their impact on the residual resistivity should be considerably reduced when the thickness of the film increases due to the reduction of the relative amount of defects.

(iv) The extracted Debye temperature values (Θ_D) reported in Table III are in excellent agreement with the 479.4 K theoretical value calculated from the Debye model [36] using the Co_2MnSi bulk modulus obtained from DFT calculations by Amari *et al.* [37] (see the supplementary information section 4 for more details). This result is mandatory to validate the model and demonstrates the robustness of this analysis.

(v) Better fitting was obtained when including the magnonic term which allowed us to extract Δ values, i.e. the distance between E_F and the minority-spin conduction band minimum (E_{CBM}). We obtain $\Delta \cong 0.3 \pm 0.1$ eV. Since the half spin gap from the minority spin valence band to E_F was measured around 0.3 - 0.4 eV in similar samples by using Spin Resolved Photoemission Spectroscopy (SR-PES) [14], this leads to a spin gap roughly equal to 0.6 eV, which is in excellent agreement with *ab initio* calculation values around 0.35 - 0.82 eV [2,38,39].

It is worth to mention a particular feature that was only observed in the resistivity of the 4 nm Co_2MnSi film. Below 20 K, an upturn in the resistivity was observed for this sample (inset of Fig. 3a). This increase of resistivity at low temperature has already been reported in $Co_2MnSi_{1-x}Al_x$ Heusler compounds, and has been ascribed to a weak localization phenomenon, due to the enhanced coherent backscattering of conduction electrons as a result of disorder in this system [32]. Such disorder can originate from chemical disorder or/and the presence of crystallographic defects. Indeed, dislocation cores were observed on our samples at the Co_2MnSi/MgO interface (Fig. 1e) as expected due to the lattices misfit [40]. These dislocations cores thus induce some local disorder mainly at the interface, that is expected to become more relevant with the reduction of the film thickness. Nevertheless, other contributions relevant at low temperatures for very low thicknesses cannot be excluded such as enhanced electron-electron interaction (EEI)

[41]. To disentangle these contributions for this particular thickness is beyond the scope of this study.

3.2. Anisotropic Magnetoresistance

Anisotropic magnetoresistance (AMR) is a phenomenon observed in ferromagnetic materials as a result of spin-orbit interaction. It manifests as a variation in the resistivity of the film with the relative orientation of the magnetization and current, and is generally defined as:

$$\mathrm{AMR} = \frac{\Delta\rho}{\rho} = \frac{\rho_{\parallel} - \rho_{\perp}}{\rho_{\perp}} \tag{6}$$

where $\rho_{\parallel}$ and $\rho_{\perp}$ are the resistivities of the film when the magnetic field is parallel to the current direction and perpendicular to the current direction, respectively.

While most common ferromagnets like Co, Ni, Fe and their alloys possess positive AMR ratios, in the case of half-metallic ferromagnets negative values have been typically reported. This can be understood under the theoretical model developed by Kodako *et al.* [42] where general expressions are obtained for the resistivity and AMR by specifying the spin state ($\sigma =\uparrow$ or $\downarrow$) of conduction s-states in s-d scattering. In this model, a relation is obtained between the sign of AMR and the dominant s-d scattering process. When s-d scattering occurs predominantly between states of different spin ($s^{\uparrow}$ to $d^{\downarrow}$ or $s^{\downarrow}$ to $d^{\uparrow}$) the sign of AMR tends to be positive ($\rho_{\parallel} > \rho_{\perp}$) and when it occurs predominantly between states of the same spin ($s^{\uparrow}$ to $d^{\uparrow}$ or $s^{\downarrow}$ to $d^{\downarrow}$) AMR tends to be negative ($\rho_{\parallel} < \rho_{\perp}$). Since HMF possess a null density of states (DOS) at the Fermi energy here for spin-down electrons (but it is also true for HMF with a spin gap in the majority spin bands), AMR should be always negative. Therefore, AMR measurements can provide a signature for half metallicity.

An example of a magneto-resistivity measurement performed on a 13 nm thick Co_2MnSi film is shown in Fig. 4a with the magnetic field being applied parallel to the current direction (black line) or perpendicular to the current direction (red line). The AMR curves for the entire thickness series can be found in the supplementary information section (Figure S5). Two peaks were observed at the coercive field (H_c) when the magnetic field was reversed back and forward for all the samples [43]. AMR ratios measured on the Co_2MnSi series are reported in Fig. 4b, together with some reference values for comparison. Negative AMR ratios were obtained for the whole thickness range, which confirms the half-metallic nature of our Co_2MnSi films (see Table IV). The AMR values obtained here can be compared with the best values reported in the literature for Co_2MnSi proving the excellent quality of our films (Fig. 4b). An increase of $|\Delta\rho| = |\rho_{\parallel} - \rho_{\perp}|$ is observed when the film thickness is reduced below the electron mean free path (see Fig. 4c) in agreement with the study of Dieny *et al*. [44]. However, the increase of film resistivity due to the increase of electron diffuse scattering at the outer film surfaces dominates causing a reduction of the AMR ratio at lower thicknesses.

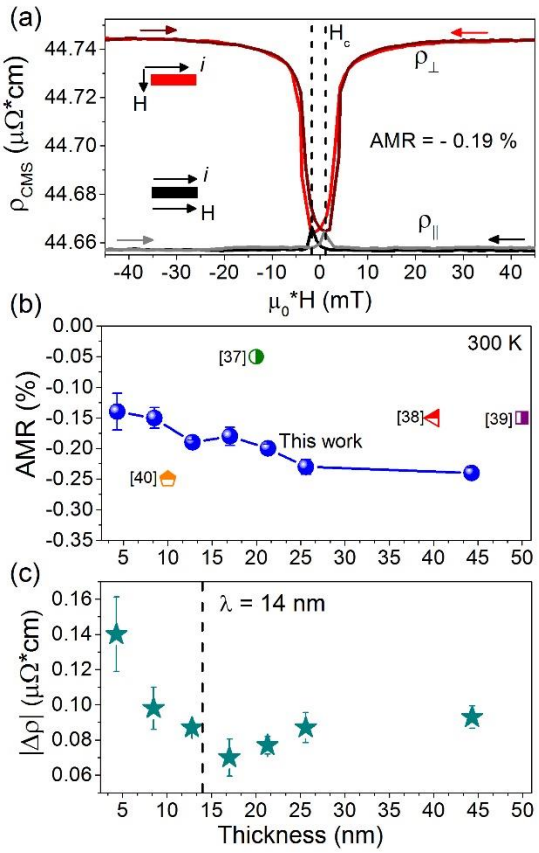

Fig. 4. Anisotropic magnetoresistance measurements. (a) Magnetoresistance vs. magnetic field for a 13 nm thick Co_2MnSi film, with the magnetic field oriented perpendicular (red line) or parallel (black line) to the current direction. (b) AMR ratio vs. CMS thickness for our samples (blue circles) and some reference values taken from the literature for comparison (other symbols) [45–48]. (c) $\Delta\rho$ vs. thickness. The dotted vertical line indicates the CMS electron mean free path determined in this study.

3.3. Hall Effect Measurements

The field dependence of Hall resistivity (ρ_{xy}) for Co_2MnSi films is shown in Fig. 5a. At high magnetic fields (applied perpendicular to the film), above saturation a small negative slope is observed as a result of the Lorentz force experienced by the carriers under the action of an external magnetic field, that is, the ordinary Hall effect. On the other hand, a steeper linear dependency is observed in the low field region, arising from the anomalous Hall effect (AHE). The origin of AHE is the spin-orbit coupling of conduction electrons in ferromagnetic materials

which produces an additional deviation of electron trajectories perpendicular to the current and the external magnetic field. The total Hall resistivity for a ferromagnet taking both terms into account can be described by the empirical formula [49]:

$$\rho_{xy} = \mu_0 \mathcal{R}_{HE} H + \mu_0 \mathcal{R}_{AHE} M_Z(H) \quad (7)$$

where μ_0 is the vacuum permeability, $\mathcal{R}_{HE}$ the ordinary Hall coefficient, $\mathcal{R}_{AHE}$ the anomalous Hall coefficient, H the external magnetic field along z direction and $M_Z(H)$ the magnetization of the film along z direction (see supplementary information section 6 for more details).

At high magnetic fields above saturation (>1.5 T) the second term in eq. (7) is constant which allows us to extract the ordinary Hall coefficient $\mathcal{R}_{HE}$ from the linear fit of $\rho_{xy}(\mu_0 H)$ (see Table IV). From the $\mathcal{R}_{HE}$ values we can determine the carrier concentration (n) by using the single parabolic band model $n = 1/e\, \mathcal{R}_{HE}$. The negative slope is consistent with electrons being the main charge carriers in this material. The carrier concentration is close to $1 * 10^{23}\ cm^{-3}$ and no significant variation was observed within the sample series. The carrier mobility was determined using $\mu = \mathcal{R}_{HE}/\rho_{xx}$ with values ranging from 0.6 to 1.5 $cm^2/V\ s$ (see Table IV). The decrease of electron mobility for lower thickness results from the increase of inelastic electron scattering as the film thickness is reduced below the electron mean free path.

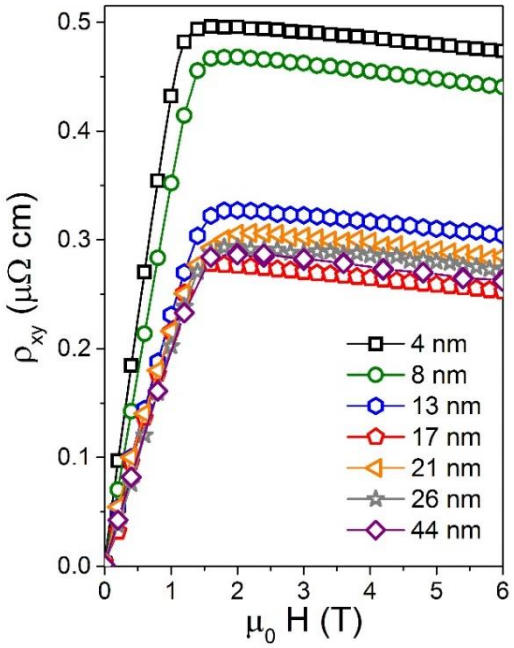

Fig. 5. Hall effect measurements. Field dependence of the Hall resistivity (ρ_{xy}) for the Co_2MnSi thickness series.

The anomalous Hall coefficient $\mathcal{R}_{AHE}$ can be extracted from the linear fit of ρ_{xy} vs. $\mu_0\, H$ in the low magnetic field regime below saturation (< 1 T). In this region, in which a linear dependency exists between the magnetization and the external magnetic field, we can write: $M_z = \eta\, H$, with $\eta = M_s/H_{sat}$, where M_s is the saturation magnetization and H_{sat} the field required to saturate the magnetization out of the plane. The parameter η was determined by fitting the out-of-plane magnetization curves of the samples (see supplementary information Figure S4b) in the low magnetic field region. Then, we can rewrite eq. 7 as follows,

$$\rho_{xy} = (\mathcal{R}_{HE} + \eta\, \mathcal{R}_{AHE})\, \mu_0\, H \qquad (8)$$

and since the ordinary Hall coefficient $\mathcal{R}_{HE}$ is already known the determination of the anomalous Hall coefficient $\mathcal{R}_{AHE}$ is straightforward. It is worth to mention that the values of η were very close to 1 for all the samples, as expected for thin film with negligible magnetocristalline anisotropy (see details in supplementary information section 7). The values of $\mathcal{R}_{AHE}$ obtained

for the different Co_2MnSi films are reported in Table IV. As can be seen, the anomalous Hall coefficient is two orders of magnitude higher than the ordinary Hall coefficient and it decreases with the increase of film thickness. To quantify the anomalous Hall effect, we calculated the anomalous Hall angle, $\theta_{AHE} = \rho_{xy}^{AHE}/\rho_{xx}$, where ρ_{xx} is the longitudinal resistivity and ρ_{xy}^{AHE} is the anomalous Hall resistivity (see details in supplementary information section 8). The anomalous Hall angles obtained at saturation for all the thickness series are reported in Table IV. Small anomalous Hall angles were obtained compared with the Co_2MnGa Heusler compound, which has been widely studied in the literature and for which a large θ_{AHE} of ~10 % have been reported [50–52]. This can be explained by the weaker spin-orbit coupling in the Co_2MnSi compound linked to its lower magnetocrystalline anisotropy compared to Co_2MnGa.

Table IV. Review of the AMR and Hall measurements performed on the Co_2MnSi thickness series at room temperature: films thickness (t), AMR values, ordinary ($\mathcal{R}_{HE}$) and anomalous ($\mathcal{R}_{AHE}$) Hall coefficients, carrier concentration (n), carrier mobility (μ) and anomalous Hall angle (θ_{AHE}) (relative error ~ 5 %).

t (nm)	AMR (%)	$\mathcal{R}_{HE}$ (10^{-3} μΩ cm/T)	n (10^{23} cm^{-3})	μ (cm^2/V s)	$\mathcal{R}_{AHE}$ (10^{-1} μΩ cm/T)	θ_{AHE} (%)
4	-0.14 ± 0.03	5.97 ± 0.05	1.05 ± 0.02	0.67 ± 0.05	4.7 ± 0.05	0.65
8	-0.15 ± 0.02	7.20 ± 0.05	0.87 ± 0.01	1.21 ± 0.03	3.5 ± 0.02	0.75
13	-0.190 ± 0.008	6.21 ± 0.08	1.01 ± 0.01	1.38 ± 0.03	2.25 ± 0.03	0.64
17	-0.190 ± 0.02	6.03 ± 0.02	1.03 ± 0.03	1.61 ± 0.03	2.22 ± 0.12	0.74
21	-0.20 ± 0.01	6.5 ± 0.3	0.96 ± 0.04	1.70 ± 0.08	2.19 ± 0.08	0.52
26	-0.23 ± 0.01	5.93 ± 0.2	1.05 ± 0.04	1.54 ± 0.06	1.99 ± 0.03	0.64
44	-0.24 ± 0.009	6.72 ± 0.3	0.93 ± 0.04	1.84 ± 0.09	1.85 ± 0.01	0.60

These measurements were also performed in the 5 – 300 K temperature range to test and better understand the underlying physics in these films. The evolution of Hall coefficients, carrier concentration and carrier mobility with temperature are shown in Fig. 6. When the temperature rises, the carrier concentration slightly increases while the carrier mobility decreases (Fig. 6 b, c). The decreasing carrier mobility can be explained by the increase of electron-phonon scattering

with increasing temperature. On the other hand, the increase of the carrier concentration is puzzling since it is expected to be constant for a metal. As these HMF materials are in between normal metals and semiconductors due to the existence of the minority spin gap, a rough explanation should be the increase of the minority spin carrier concentration with temperature. However, the thermal energy at 300 K is considerably smaller than the Co_2MnSi spin gap (0.35 - 0.8 eV [2,38,39]). A better explanation would be based on the complex Fermi surfaces with the coexistence of electrons and holes in these Heusler HMF materials [32]. In that way, the parabolic single-band model employed here to calculate n and μ cannot completely describe the situation of Heusler compounds. Therefore, the values of n and μ reported in this study represent effective values associated to the predominant type of carriers in this material.

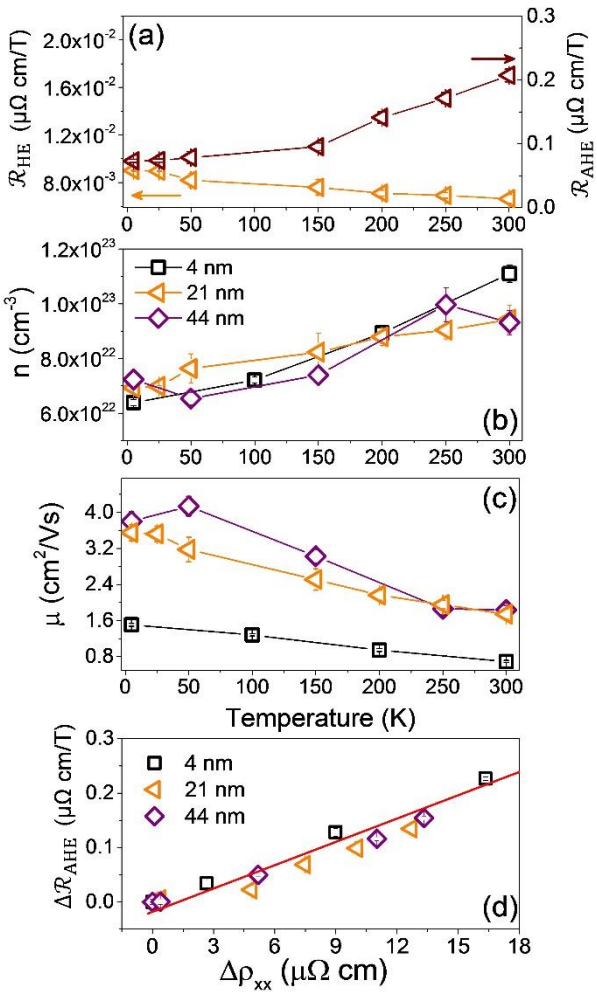

Fig. 6. Transport properties of the CMS films. (a) Normal and anomalous Hall coefficients, (b) CMS carrier concentration and (c) carrier mobility versus temperature for samples of different thickness. (d) Scaling of AHE coefficient for CMS films of different thickness derived from the Hall measurements performed at different temperatures from 5 - 300 K.

Contrary to the ordinary Hall coefficient, the anomalous Hall effect coefficient increases with temperature. In fact, this temperature dependence arises from the temperature dependence of longitudinal resistivity since $\mathcal{R}_{AHE}(T) \propto \rho_{xx}^{\alpha}(T)$, where the α exponent gives information on the main scattering mechanism. An $\alpha = 1$ exponent is usually assigned to skew scattering, i.e. an extrinsic effect resulting from the asymmetry of the electron scattering cross-section due to spin-

orbit interaction. On the other hand, $\alpha = 2$ can be the signature of another extrinsic effect known as side-jump scattering or to the intrinsic Berry phase-related mechanism [53]. The longitudinal resistivity of the entire Co_2MnSi thickness series places Co_2MnSi in the good-metal regime ($1 < \rho < 10^2\ \mu\Omega\ cm$) [53]. Studies performed on common ferromagnets like Co and Fe have suggested that side-jump and intrinsic scattering mechanisms predominate in this regime at low temperatures [53]. In this work, the change of the films' resistivity with temperature and thickness provides an ideal scenario to explore the AHE scaling in Co_2MnSi and to identify the dominant scattering mechanism. In Fig. 6d, $\Delta\mathcal{R}_{AHE} = \mathcal{R}_{AHE}(T) - \mathcal{R}_{AHE}(5\ K)$ versus $\Delta\rho_{xx} = \rho_{xx}(T) - \rho_{xx}(5\ K)$ is plotted and a linear trend ($\alpha = 1$) was observed suggesting that skew scattering is the dominant temperature-dependent scattering mechanism taking place in the Co_2MnSi films, even in the good-metal regime.

4. DISCUSSION AND CONCLUSIONS

In summary, the investigated Co_2MnSi films with ultra-low magnetic damping allowed us to extract important and robust information on the electronic transport properties in this Half-Metal-Magnetic material. The analysis of film resistivity versus thickness allowed us to estimate the inelastic electron mean free path in these films to be equal to 14 nm at room temperature. The increase of resistivity for low thicknesses thus arises from interface scattering, but possibly also from misfit dislocations. This mean free path is an important parameter to consider towards the fabrication of magnetoresistive devices with Co_2MnSi electrodes. The temperature dependence of the films' resistivity indicates that s-d electron-phonon scattering is the main scattering mechanism contributing to the film resistivity from 50 to 300 K. This analysis is enforced by the excellent agreement between the Debye temperature extracted from the resistivity curve fits (478 ± 9 K) with the calculated one based on Co_2MnSi elastic constants in the bulk (479.4 K). In

addition, the introduction of an exponential decrease to the typical T^2 dependence from electron-magnon scattering allows us to determine the distance between the Fermi energy and the first available states at the minority-spin conduction band, i.e. the half-spin gap above the Fermi energy. As the half-spin gap between the minority spin valence band and the Fermi energy was known from SR-PES measurements, a total gap around 0.6 eV is obtained in agreement with *ab initio* calculations [2,38,39]. This half-metallicity is confirmed by the negatives AMR ratios obtained for the entire thickness series. This demonstrates that performing transport measurements is a good method to verify the half-metallicity of Heusler compounds.

Furthermore, Hall measurements confirm that electrons are the main charge carrier in Co_2MnSi, and allowed us to determine the electron concentration and electron mobility. The electron mobility is observed to decrease when decreasing film thickness, due to an enhancement of inelastic scattering at the film surface (and probably also at dislocation defects) when the thickness is reduced below the electron mean free path; while the electron concentration seems not to change appreciably. The electron mobility was observed to decrease with temperature as a result of the increase in phonon-electron scattering. However, a slight increase of the carrier concentration with temperature is observed and probably needs *ab initio* calculations to be explained. Finally, the evolution of the films' resistivity with thickness and temperature provides the ideal scenario for studying the scaling of the Hall resistivity with the longitudinal resistivity, indicating that skew scattering is the predominant temperature-dependent scattering mechanism taking place in Co_2MnSi. Finally, we may go as far as to say that all the transport parameters reported here are robust and characteristic of HMF Co_2MnSi thin films with ultra-low magnetic damping. This may be very useful in views of the implementation of Co_2MnSi films in magnetoresistive devices.

Acknowledgments

We would like to thanks Sylvie Migot and Jaafar Ghanbaja for the FIB preparation and TEM imaging.

Funding sources

This work was carried out in the context of the research project CHIPMuNCS, founded by the Agence Nationale de la Recherche (Contract No. ANR-17-CE24-0008). This work was also partially supported from the French PIA project "Lorraine Université d'Excellence", reference ANR-15IDEX-04-LUE. Devices in the present study were patterned at MiNaLor clean-room platform which is partially supported by FEDER and Grand Est Region through the RaNGE project.

Data availability

The raw/processed data required to reproduce these findings cannot be shared at this time as the data also forms part of an ongoing study.

References

[1] F. Heusler, Über die Synthese ferromagnetischer Manganlegierungen, Verhandlungen Dtsch. Phys. Ges. 5 (1903) 219.

[2] I. Galanakis, P. Mavropoulos, Spin-polarization and electronic properties of half-metallic Heusler alloys calculated from first principles, J. Phys. Condens. Matter. 19 (2007) 315213. https://doi.org/10.1088/0953-8984/19/31/315213.

[3] T. Graf, C. Felser, S.S.P. Parkin, Simple rules for the understanding of Heusler compounds, Prog. Solid State Chem. 39 (2011) 1–50. https://doi.org/10.1016/j.progsolidstchem.2011.02.001.

[4] S. Mallick, S. Mondal, T. Seki, S. Sahoo, T. Forrest, F. Maccherozzi, Z. Wen, S. Barman, A. Barman, K. Takanashi, S. Bedanta, Tunability of Domain Structure and Magnonic Spectra in

Antidot Arrays of Heusler Alloy, Phys. Rev. Appl. 12 (2019) 014043. https://doi.org/10.1103/PhysRevApplied.12.014043.

[5] H. Lin, L.A. Wray, Y. Xia, S. Xu, S. Jia, R.J. Cava, A. Bansil, M.Z. Hasan, Half-Heusler ternary compounds as new multifunctional experimental platforms for topological quantum phenomena, Nat. Mater. 9 (2010) 546–549. https://doi.org/10.1038/nmat2771.

[6] S. Chadov, X. Qi, J. Kübler, G.H. Fecher, C. Felser, S.C. Zhang, Tunable multifunctional topological insulators in ternary Heusler compounds, Nat. Mater. 9 (2010) 541–545. https://doi.org/10.1038/nmat2770.

[7] C. Banerjee, N. Teichert, K. Siewierska, Z. Gercsi, G. Atcheson, P. Stamenov, K. Rode, J.M.D. Coey, J. Besbas, Single pulse all-optical toggle switching of magnetization without Gd: The example of Mn_2Ru_xGa, (2019). https://arxiv.org/abs/1909.05809v2 (accessed July 2, 2020).

[8] R.A. de Groot, F.M. Mueller, P.G. van Engen, K.H.J. Buschow, New Class of Materials: Half-Metallic Ferromagnets, Phys. Rev. Lett. 50 (1983) 2024–2027. https://doi.org/10.1103/PhysRevLett.50.2024.

[9] Y. Sakuraba, K. Takanashi, Giant Magnetoresistive Devices with Half-Metallic Heusler Compounds, in: C. Felser, A. Hirohata (Eds.), Heusler Alloys Prop. Growth Appl., Springer International Publishing, Cham, 2016: pp. 389–400. https://doi.org/10.1007/978-3-319-21449-8_16.

[10] A. Sakuma, First-principles study of the Gilbert damping constants of Heusler alloys based on the torque correlation model, J. Phys. Appl. Phys. 48 (2015) 164011. https://doi.org/10.1088/0022-3727/48/16/164011.

[11] C. Liu, C.K.A. Mewes, M. Chshiev, T. Mewes, W.H. Butler, Origin of low Gilbert damping in half metals, Appl. Phys. Lett. 95 (2009) 022509. https://doi.org/10.1063/1.3157267.

[12] M.S. Gabor, T. Petrisor, M. Nasui, M.A. Nsibi, J. Nath, I.M. Miron, Spin-orbit Torques and Magnetization Switching in Perpendicularly Magnetized Epitaxial $Pd/Co_2FeAl/MgO$ Structures, Phys. Rev. Appl. 13 (2020) 054039. https://doi.org/10.1103/PhysRevApplied.13.054039.

[13] A. Hirohata, J. Sagar, L.R. Fleet, S.S.P. Parkin, Heusler Alloy Films for Spintronic Devices, in: C. Felser, A. Hirohata (Eds.), Heusler Alloys Prop. Growth Appl., Springer International Publishing, Cham, 2016: pp. 219–248. https://doi.org/10.1007/978-3-319-21449-8_9.

[14] C. Guillemard, S. Petit-Watelot, L. Pasquier, D. Pierre, J. Ghanbaja, J.-C. Rojas-Sánchez, A. Bataille, J. Rault, P. Le Fèvre, F. Bertran, S. Andrieu, Ultralow Magnetic Damping in Co_2Mn-Based Heusler Compounds: Promising Materials for Spintronics, Phys. Rev. Appl. 11 (2019) 064009. https://doi.org/10.1103/PhysRevApplied.11.064009.

[15] S. Trudel, O. Gaier, J. Hamrle, B. Hillebrands, Magnetic anisotropy, exchange and damping in cobalt-based full-Heusler compounds: an experimental review, J. Phys. Appl. Phys. 43 (2010). https://doi.org/10.1088/0022-3727/43/19/193001.

[16] S. Husain, S. Akansel, A. Kumar, P. Svedlindh, S. Chaudhary, Growth of Co_2FeAl Heusler alloy thin films on Si(100) having very small Gilbert damping by Ion beam sputtering, Sci. Rep. 6 (2016). https://doi.org/DOI: 10.1038/srep28692.

[17] H.T. Nembach, T.J. Silva, J.M. Shaw, M.L. Schneider, M.J. Carey, S. Maat, J.R. Childress, Perpendicular ferromagnetic resonance measurements of damping and Landé g-factor in sputtered $(Co_2Mn)_{1-x}Ge_x$ thin films, Phys. Rev. B. 84 (2011) 054424. https://doi.org/10.1103/PhysRevB.84.054424.

[18] Y.-C. Chen, M. Yen, Y.-H. Lai, A. Markou, L. Zhang, Y.-Y. Chin, H.-J. Lin, C.-T. Chen, C. Felser, Y.-H. Chu, Heteroepitaxy of Co-Based Heusler Compound/Muscovite for Flexible Spintronics, ACS Appl. Mater. Interfaces. 11 (2019) 35162–35168. https://doi.org/10.1021/acsami.9b12219.

[19] M. Jourdan, J. Minár, J. Braun, A. Kronenberg, S. Chadov, B. Balke, A. Gloskovskii, M. Kolbe, H.J. Elmers, G. Schönhense, H. Ebert, C. Felser, M. Kläui, Direct observation of half-metallicity in the Heusler compound Co_2MnSi, Nat. Commun. 5 (2014) 3974. https://doi.org/10.1038/ncomms4974.

[20] S. Andrieu, A. Neggache, T. Hauet, T. Devolder, A. Hallal, M. Chshiev, A.M. Bataille, P. Le Fèvre, F. Bertran, Direct evidence for minority spin gap in the Co_2MnSi Heusler compound, Phys. Rev. B. 93 (2016) 094417. https://doi.org/10.1103/PhysRevB.93.094417.

[21] H. Liu, Y. Honda, T. Taira, K. Matsuda, M. Arita, T. Uemura, M. Yamamoto, Giant tunneling magnetoresistance in epitaxial $Co_2MnSi/MgO/Co_2MnSi$ magnetic tunnel junctions by half-metallicity of Co_2MnSi and coherent tunneling, Appl. Phys. Lett. 101 (2012) 132418. https://doi.org/10.1063/1.4755773.

[22] Y. Sakuraba, K. Izumi, T. Iwase, S. Bosu, K. Saito, K. Takanashi, Y. Miura, K. Futatsukawa, K. Abe, M. Shirai, Mechanism of large magnetoresistance in $Co_2MnSi/Ag/Co_2MnSi$ devices

with current perpendicular to the plane, Phys. Rev. B. 82 (2010) 094444. https://doi.org/10.1103/PhysRevB.82.094444.

[23] C. Guillemard, S. Petit-Watelot, T. Devolder, L. Pasquier, P. Boulet, S. Migot, J. Ghanbaja, F. Bertran, S. Andrieu, Issues in growing Heusler compounds in thin films for spintronic applications, J. Appl. Phys. 128 (2020) 241102. https://doi.org/10.1063/5.0014241.

[24] F.C. Frank, J.H. van der Merwe, N.F. Mott, One-dimensional dislocations. I. Static theory, Proc. R. Soc. Lond. Ser. Math. Phys. Sci. 198 (1949) 205–216. https://doi.org/10.1098/rspa.1949.0095.

[25] Y. Frenkel, T. Kontorova, J. Phys. Acad. Sci. USSR. 1 (1939) 137.

[26] M.A.W. Schoen, D. Thonig, M.L. Schneider, T.J. Silva, H.T. Nembach, O. Eriksson, O. Karis, J.M. Shaw, Ultra-low magnetic damping of a metallic ferromagnet, Nat. Phys. 12 (2016) 839–842. https://doi.org/10.1038/nphys3770.

[27] J.M. Shaw, E.K. Delczeg-Czirjak, E.R.J. Edwards, Y. Kvashnin, D. Thonig, M.A.W. Schoen, M. Pufall, M.L. Schneider, T.J. Silva, O. Karis, K.P. Rice, O. Eriksson, H.T. Nembach, Magnetic damping in sputter-deposited Co_2MnGe Heusler compounds with A2, B2, and $L2_1$ orders: Experiment and theory, Phys. Rev. B. 97 (2018) 094420. https://doi.org/10.1103/PhysRevB.97.094420.

[28] M.A.W. Schoen, J.M. Shaw, H.T. Nembach, M. Weiler, T.J. Silva, Radiative damping in waveguide-based ferromagnetic resonance measured via analysis of perpendicular standing spin waves in sputtered permalloy films, Phys. Rev. B. 92 (2015) 184417. https://doi.org/10.1103/PhysRevB.92.184417.

[29] V. Flovik, F. Macià, A.D. Kent, E. Wahlström, Eddy current interactions in a ferromagnet-normal metal bilayer structure, and its impact on ferromagnetic resonance lineshapes, J. Appl. Phys. 117 (2015) 143902. https://doi.org/10.1063/1.4917285.

[30] E.H. Sondheimer, The mean free path of electrons in metals, Adv. Phys. 1 (1952) 1–42. https://doi.org/10.1080/00018735200101151.

[31] W.H. Wang, X.B. Ren, G.H. Wu, M. Przybylski, J. Barthel, J. Kirschner, Magnetic and transport properties of epitaxial Co_2MnSi films, IEEE Trans. Magn. 41 (2005) 2805–2807. https://doi.org/10.1109/TMAG.2005.854833.

[32] J.C. Prestigiacomo, D.P. Young, P.W. Adams, S. Stadler, Hall effect and the magnetotransport properties of $Co_2MnSi_{1-x}Al_x$ Heusler alloys, J. Appl. Phys. 115 (2014) 043712. https://doi.org/10.1063/1.4862966.

[33] D. Bombor, C.G.F. Blum, O. Volkonskiy, S. Rodan, S. Wurmehl, C. Hess, B. Büchner, Half-Metallic Ferromagnetism with Unexpectedly Small Spin Splitting in the Heusler Compound Co_2FeSi, Phys. Rev. Lett. 110 (2013) 066601. https://doi.org/10.1103/PhysRevLett.110.066601.

[34] A. Barry, J.M.D. Coey, L. Ranno, K. Ounadjela, Evidence for a gap in the excitation spectrum of CrO_2, J. Appl. Phys. 83 (1998) 7166–7168. https://doi.org/10.1063/1.367791.

[35] A.H. Wilson, The Electrical Conductivity of the Transition Metals, Proc. R. Soc. Lond. Ser. Math. Phys. Sci. 167 (1938) 580–593.

[36] O.L. Anderson, A simplified method for calculating the debye temperature from elastic constants, J. Phys. Chem. Solids. 24 (1963) 909–917. https://doi.org/10.1016/0022-3697(63)90067-2.

[37] S. Amari, R. Mebsout, S. Méçabih, B. Abbar, B. Bouhafs, First-principle study of magnetic, elastic and thermal properties of full Heusler Co_2MnSi, Intermetallics. 44 (2014) 26–30. https://doi.org/10.1016/j.intermet.2013.08.009.

[38] B. Pradines, R. Arras, I. Abdallah, N. Biziere, L. Calmels, First-principles calculation of the effects of partial alloy disorder on the static and dynamic magnetic properties of Co_2MnSi, Phys. Rev. B. 95 (2017) 094425. https://doi.org/10.1103/PhysRevB.95.094425.

[39] S. Picozzi, A. Continenza, A.J. Freeman, Co_2MnX (X=Si, Ge, Sn) Heusler compounds: An ab initio study of their structural, electronic, and magnetic properties at zero and elevated pressure, Phys. Rev. B. 66 (2002) 094421. https://doi.org/10.1103/PhysRevB.66.094421.

[40] I.V. Markov, Crystal Growth For Beginners: Fundamentals Of Nucleation, Crystal Growth And Epitaxy (Third Edition), World Scientific Publishing Co. Pte. Ltd., Singapore, 2016.

[41] P.A. Lee, T.V. Ramakrishnan, Disordered electronic systems, Rev. Mod. Phys. 57 (1985) 287–337. https://doi.org/10.1103/RevModPhys.57.287.

[42] S. Kokado, M. Tsunoda, K. Harigaya, A. Sakuma, Anisotropic Magnetoresistance Effects in Fe, Co, Ni, Fe_4N, and Half-Metallic Ferromagnet: A Systematic Analysis, J. Phys. Soc. Jpn. 81 (2012) 024705. https://doi.org/10.1143/JPSJ.81.024705.

[43] B. Hong, Y. Yang, J. Zhao, K. Hu, J. Peng, H. Zhang, W. Liu, Z. Luo, H. Huang, X. Li, C. Gao, Quantifying electric-field control of magnetization rotation in Ni/SiO_2/Ti/(011)-PMN-PT multiferroic heterostructures via anisotropic magnetoresistance measurements, Mater. Lett. 169 (2016) 110–113. https://doi.org/10.1016/j.matlet.2016.01.109.

[44] B. Dieny, M. Li, S.H. Liao, C. Horng, K. Ju, Effect of interfacial specular electron reflection on the anisotropic magnetoresistance of magnetic thin films, J. Appl. Phys. 88 (2000) 4140–4145. https://doi.org/10.1063/1.1310189.

[45] M. Oogane, A.P. McFadden, Y. Kota, T.L. Brown-Heft, M. Tsunoda, Y. Ando, C.J. Palmstrøm, Fourfold symmetric anisotropic magnetoresistance in half-metallic Co_2MnSi Heusler alloy thin films, Jpn. J. Appl. Phys. 57 (2018) 063001. https://doi.org/10.7567/JJAP.57.063001.

[46] T. Sato, S. Kokado, S. Kosaka, T. Ishikawa, T. Ogawa, M. Tsunoda, Large negative anisotropic magnetoresistance in Co_2MnGa Heusler alloy epitaxial thin films, Appl. Phys. Lett. 113 (2018) 112407. https://doi.org/10.1063/1.5047821.

[47] Y. Sakuraba, S. Kokado, Y. Hirayama, T. Furubayashi, H. Sukegawa, S. Li, Y.K. Takahashi, K. Hono, Quantitative analysis of anisotropic magnetoresistance in Co_2MnZ and Co_2FeZ epitaxial thin films: A facile way to investigate spin-polarization in half-metallic Heusler compounds, Appl. Phys. Lett. 104 (2014) 172407. https://doi.org/10.1063/1.4874851.

[48] M. Oogane, A.P. McFadden, K. Fukuda, M. Tsunoda, Y. Ando, C.J. Palmstrøm, Low magnetic damping and large negative anisotropic magnetoresistance in half-metallic $Co_{2-x}Mn_{1+x}Si$ Heusler alloy films grown by molecular beam epitaxy, Appl. Phys. Lett. 112 (2018) 262407. https://doi.org/10.1063/1.5030341.

[49] M. Obaida, K. Westerholt, H. Zabel, Magnetotransport properties of Cu_2MnAl, Co_2MnGe, and Co_2MnSi Heusler alloy thin films: From nanocrystalline disordered state to long-range-ordered crystalline state, Phys. Rev. B. 84 (2011) 184416. https://doi.org/10.1103/PhysRevB.84.184416.

[50] Y. Zhang, Y. Yin, G. Dubuis, T. Butler, N.V. Medhekar, S. Granville, Berry curvature origin of the thickness-dependent anomalous Hall effect in a ferromagnetic Weyl semimetal, Npj Quantum Mater. 6 (2021) 1–8. https://doi.org/10.1038/s41535-021-00315-8.

[51] K. Manna, L. Muechler, T.-H. Kao, R. Stinshoff, Y. Zhang, J. Gooth, N. Kumar, G. Kreiner, K. Koepernik, R. Car, J. Kübler, G.H. Fecher, C. Shekhar, Y. Sun, C. Felser, From Colossal

to Zero: Controlling the Anomalous Hall Effect in Magnetic Heusler Compounds via Berry Curvature Design, Phys. Rev. X. 8 (2018) 041045. https://doi.org/10.1103/PhysRevX.8.041045.

[52] J. Chen, H. Li, B. Ding, H. Zhang, E. Liu, W. Wang, Large anomalous Hall angle in a topological semimetal candidate TbPtBi, Appl. Phys. Lett. 118 (2021) 031901. https://doi.org/10.1063/5.0033707.

[53] N. Nagaosa, J. Sinova, S. Onoda, A.H. MacDonald, N.P. Ong, Anomalous Hall effect, Rev. Mod. Phys. 82 (2010) 1539–1592. https://doi.org/10.1103/RevModPhys.82.1539.